Editors' Suggestion

Classification of local chemical environments from x-ray absorption spectra using supervised machine learning

Matthew R. Carbone,[1,2] Shinjae Yoo,[2] Mehmet Topsakal,[3,*] and Deyu Lu[3,*]

[1]*Department of Chemistry, Columbia University, New York, New York 10027, USA*
[2]*Computational Science Initiative, Brookhaven National Laboratory, Upton, New York 11973, USA*
[3]*Center for Functional Nanomaterials, Brookhaven National Laboratory, Upton, New York 11973, USA*

X-ray absorption spectroscopy is a premier element-specific technique for materials characterization. Specifically, the x-ray absorption near-edge structure (XANES) encodes important information about the local chemical environment of an absorbing atom, including coordination number, symmetry, and oxidation state. Interpreting XANES spectra is a key step towards understanding the structural and electronic properties of materials, and as such, extracting structural and electronic descriptors from XANES spectra is akin to solving a challenging inverse problem. Existing methods rely on empirical fingerprints, which are often qualitative or semiquantitative and not transferable. In this paper, we present a machine learning-based approach, which is capable of classifying the local coordination environments of the absorbing atom from simulated K-edge XANES spectra. The machine learning classifiers can learn important spectral features in a broad energy range without human bias and once trained, can make predictions on the fly. The robustness and fidelity of the machine learning method are demonstrated by an average 86% accuracy across the wide chemical space of oxides in eight $3d$ transition-metal families. We found that spectral features beyond the preedge region play an important role in the local structure classification problem especially for the late $3d$ transition-metal elements.

I. INTRODUCTION

Knowledge of material structures on the atomic scale is essential to understanding physical phenomena and material properties that can lead to practical applications. Specifically, key information about the local chemical environment (LCE) surrounding an atom, including symmetry, coordination number, bond length, and bond angle, forms the fundamental basis that determines the electronic properties of materials. In order to resolve the structure-property relationship, the characterization of atomic structures and their dynamic changes under different thermodynamic conditions have become a primary target of experimental studies. Such efforts have made tremendous impacts on many research fields, including superconductivity [1], ultrafast dynamics [2], energy storage [3], and photocatalysis [4]. Recent progress in materials discovery using smart automation [5,6] and *in situ* and *operando* experiments [7] further highlights emerging challenges and opportunities of materials characterization in *real time*.

Among many experimental techniques (e.g., imaging, diffraction, and spectroscopy), the x-ray absorption near-edge structure (XANES) is a premier tool for probing LCEs because it is element specific, sensitive to local structural and electronic properties, and applicable under harsh experimental conditions [8–10], making it a robust structure refinement method [8,11–15]. Given the atomic arrangement of a sample (**x**), its XANES spectra (**y**) can be determined through quantum-mechanical laws (f) via the mapping $\mathbf{y} = f(\mathbf{x})$. Extracting the information of the LCE ($\tilde{\mathbf{x}}$) as a subset of **x** from spectral data can be formulated as an inverse problem: $\tilde{\mathbf{x}} = f^{-1}(\mathbf{y})$. The solution of this inverse problem is highly nontrivial because the spectral information in experimental XANES is not only abstract, but also averaged over the whole sample. Consequently, much of the success in the past has been achieved by using fingerprints established from empirical observations.

In this paper, we focus on $3d$ transition-metal K-edge XANES, which carries rich information about the electronic transitions from the $1s$ core level of the absorbing atom to unoccupied states. Since the 1940s, extensive research has been carried out to correlate spectral features of K-edge XANES spectra, especially in the preedge region, to LCEs [16,17]. For example, Hanson and Beeman [18] observed distinct chemical shifts in the absorption edge of Mn K-edge XANES in Mn, MnS, MnO_2, and $KMnO_4$. Wong *et al.* [19] showed linear relationships between the oxidation state of V and both the preedge and the absorption-edge positions in the K edge. Farges and co-workers [20–22] and Jackson *et al.* [23] conducted comprehensive studies of the correlation between the preedge features and the coordination number in Ti, Fe, and Ni compounds; they found that the preedge peak intensity decreases with increasing coordination number. For fixed coordination number, early $3d$ transition-metal elements (Ti, V, Cr, and Mn) have stronger preedge peaks than late transition-metal elements (Fe, Co, Ni, and Cu) overall [17]. Furthermore, whereas both preedge peak locations and intensities in Ti [20] and Ni species [22] exhibit a significant dependence on the coordination number, the preedge peak

_____
*Authors to whom correspondence should be addressed:
mtopsakal@bnl.gov; dlu@bnl.gov

positions in Fe compounds are independent of coordination number [23].

From a theoretical standpoint, the preedge peak intensity can be understood qualitatively from quantum-mechanical selection rules. The dominant contribution in K-edge XANES comes from $s \rightarrow p$ dipole transitions as the $s \rightarrow d$ quadrupole terms are generally orders of magnitude smaller. The density of states corresponding to the preedge regions of $3d$ transition metals are derived primarily from their empty $3d$ bands, and direct $s \rightarrow d$ transitions are dipole forbidden, which implies a vanishing peak intensity. However, preedge peak intensity is enhanced when atomic unoccupied p and d states hybridize. According to group theory, atomic p-d mixing is allowed under T_d symmetry but is forbidden under O_h symmetry [24,25]. As a result, $3d$ transition metals with tetrahedral geometries tend to exhibit stronger preedge peak intensities than those with octahedral geometries. To this end, empirical diagrams have been compiled to classify four-, five-, and six-coordinated Ti, Ni, and Fe based on preedge peak positions and intensities [20–23]; we will refer to this method as the empirical fingerprint approach.

Despite the wide range of applications of the empirical fingerprint approach, including classifying LCEs in crystals, amorphous systems [21,26], and catalysts [27], it has several limitations that may hinder its practical applications in the broader materials domain. First, coordination number is not the only factor that affects preedge peak features. Quantitative preedge features are determined by multiple factors, including coordination number, local distortion, oxidation state, and the nature of the ligands [28]. For example, local distortions, e.g., displacements from the inversion center in octahedral geometries under the crystal field can lower the local symmetry and enable atomic p-d mixing, resulting in dramatic enhancement of preedge peak intensity [28]. Such local distortion-induced preedge peak intensity enhancement has been reported in the V K edges of six-coordinated MgV_2O_6 [29] and $NaV_{10}O_{28}$ [30] and in the Ti K edge of six-coordinated $Li_4Ti_5O_{12}$ [31]. Therefore, isolating pure LCE effects and extracting robust correlations between the LCE and the simple spectral descriptors, although valid for exemplary systems, may not be feasible for more structurally complex ones.

Second, the empirical fingerprint approach relies on human knowledge to engineer spectral descriptors, which may introduce bias. For example, existing spectral descriptors are primarily derived from the preedge region (e.g., peak positions and intensities). However, it is known that preedge features are much less visible in late transition metals than early transition metals [17]. Therefore, the existing empirical fingerprint approach may not work effectively for late transition metals due to poor spectral contrast in the preedge region. One may need to systematically explore main- and postedge spectral features in order to engineer and optimize new descriptors, which may not necessarily be simple ones, to tackle this problem.

Machine learning (ML) methods are a promising candidate to solve this inverse materials characterization problem. Instead of relying on empirical features derived from a small number of human observations, ML methods are data-driven approaches that make predictions based on large training sets, eliminating human bias from the feature selection process. There are myriad successful examples of the utilization of ML

methods in condensed-matter physics, materials science, and chemistry, including methods to solve many-body problems [32], predict quantum phase transitions [33], generate force field potentials [34], design new catalysts [35], and perform structure refinement [36,37]. In the context of XANES, one expects ML algorithms to *learn* spectral descriptors in the full energy range of the spectrum and weight them appropriately for robust LCE predictions.

In this paper, we tackled the LCE classification problem using supervised ML applied to a wide energy range of the XANES spectra ($\sim$50 eV above the onset) as input. In this way, the spectral feature space was systematically explored in order to establish the relationships between XANES spectra and LCE classes, specifically the local atomic geometries. As a proof of principle, we applied ML algorithms to synthetic K-edge XANES spectra obtained from high throughput *ab initio* calculations. This paper serves as a precursor to a potentially very powerful tool for real-time structure refinement using experimental XANES, which will require in-depth understanding of the accuracy of the theory and further improvement of the ML algorithms.

II. METHODS

The workflow of the element-specific spectrum-based LCE classification framework is summarized in Fig. 1, which contains three core modules: *data acquisition*, *LCE class labeling*, and *training of machine learning models*. We stress that the workflow we developed can be adapted to a wide range of elements characterized by different spectroscopic techniques as long as the spectral information is element specific and sensitive to the LCE such that there exists distinguishable spectral contrast associated with different LCEs. Below, we describe each module in detail.

A. Data acquisition

For any given element, the first step is to extract atomic structures representing different LCEs from existing materials structure databases. The structural database must be large enough to build a reasonably sized training set for machine learning models. To demonstrate the applicability of the LCE classification framework, we have considered eight $3d$ transition-metal elements (Ti, V, Cr, Mn, Fe, Co, Ni, and Cu) and extracted all available oxide structures that have been structurally optimized using density functional theory from the Materials Project Database [38–40].

Once the structural database is established, the next step is to generate the corresponding spectral database. We focused on the K-edge XANES as it is element specific and sensitive to the LCE (e.g., symmetry, charge state, and coordination number). In principle, one may populate the spectral database entirely with experimental spectra, but this strategy suffers from several drawbacks. First, experimental XANES spectra represent an average of signals (site-averaged signals) from each absorbing site (site-specific signals). In order to identify the correlations between spectra and local structures using ML, it is necessary to use site-specific spectra for training as they possess much stronger spectral contrast than the site-averaged spectra. Second, when developing LCE
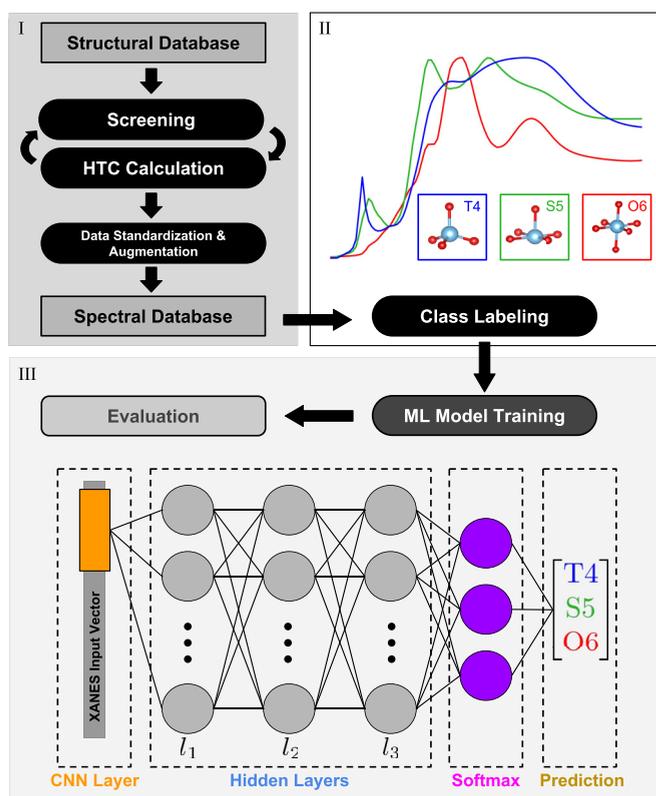
FIG. 1. Workflow of the spectrum-based local chemical environment classification framework using supervised machine learning, which contains three modules: (I) data acquisition supplemented by high throughput computing (HTC) calculations, (II) labeling, and (III) training of machine learning models. The machine learning architecture (set of hyperparameters) used in this paper is shown in Module III. Notably, the model consists of an optional convolutional layer (shown in orange) followed by three hidden layers l_1, l_2, and l_3 consisting of 90, 60, and 20 neurons, respectively, ending with a softmax output. Further details of the network are described in Sec. II C.

classifiers using supervised ML methods, one needs to label XANES spectra with LCE descriptors, which means that only experimental spectra of known structures can be selected for the database. This requirement severely limits the pool of candidates for the database to mostly well-characterized crystal structures. As a result, qualified experimental spectra represent only a small fraction of the targeting LCEs in the local configuration space, which are heavily weighted in known crystals and underrepresent the materials space of amorphous systems, surfaces, interfaces, and nanoparticles. Consequently, a pure experimental spectral database suffers from data availability and data heterogeneity issues.

On the other hand, combined with available structural databases and well-established structure sampling methods, computational XANES have a clear advantage in exploring the LCE space and producing site-specific spectra. Furthermore, recent developments in computational XANES modeling [41–51] have made it feasible to contrast experimental spectra quantitatively, enabling accurate local structure refinement of nanoparticles [36,52], interfaces [53], dopant sites

[54,55], and structural phase transformation [31,37] using computational techniques. An accurate and computationally efficient first-principles XANES method would be an ideal choice for sampling the vast LCE parameter space and mitigating data availability and heterogeneity issues. Indeed, computational XANES databases have recently emerged as a new tool for fast structure screening through data mining [56–58].

In this paper, we generated the computational XANES database with the FEFF9 code [59], which is a popular and computationally efficient method based on multiple-scattering theory. We utilized the existing site-specific x-ray absorption spectroscopy FEFF library in the Materials Project [56,57] and only calculated spectra not contained in this library. In the first data standardization step, site-specific spectra that failed sanity checks were automatically discarded, such as when the FEFF calculations did not converge with the default input or when the output FEFF spectra are not physical (e.g., with negative absorption coefficients). In the second step, we removed "duplicates," which otherwise would have introduced bias if nearly identical structures were selected for both training and testing. We used a site-symmetry finder from the PYMATGEN library [39] to determine which sites in a crystal structure are symmetrically equivalent. For every pair of spectra, one was removed from the dataset if the average mean absolute difference between them was less than 0.015, a number chosen based on visual inspection of a large number of similar spectra. The process of removing duplicates also has the benefit of reducing the total number of necessary FEFF calculations to populate the XANES database. Finally, calculated XANES spectra were spline interpolated onto an absorbing site-specific energy grid so that the input feature vector was standardized for each spectrum. For each type of absorbing site, the energy grid was chosen such that it contains the maximum amount of available information with an energy resolution of approximately 0.5 eV.

All standardized data before augmentation are henceforth referred to as the base dataset. Training data were augmented by shifting the spectra by ±1 and ±2 eV. The size of the augmented training set thus becomes five times the size of the base dataset. We found that data augmentation improves the accuracy and robustness of the machine learning model.

B. Local chemical environment class labeling

Feature engineering of LCEs is an active research topic with increasing applications in a variety of areas including, for example, neural network potential development [34,60–62]. Among many possible choices, labels based on the coordination environment (e.g., tetrahedral, square pyramidal, and octahedral geometries), although simple, provide key information on chemical bonding and have been widely used in the x-ray spectroscopy community. In this paper, we utilized the continuous symmetry measure (CSM), developed by Pinsky and Avnir [63] and hosted in the CHEMENV package [64], to measure the similarity between an input local geometry and a particular polyhedron. The smaller the CSM for a polyhedron, the more the input geometry resembles it. We applied a cutoff such that atoms further away than 1.2 times the nearest-neighbor distance from the absorbing site were

TABLE I. The distribution of classes in the structure database used for training the machine learning models.

Absorber	$T4$	$S5$	$O6$	Total
Ti	271	359	1562	2192
V	948	412	2006	3366
Cr	396	121	902	1419
Mn	502	657	2334	3493
Fe	797	319	1874	2990
Co	583	227	1428	2238
Ni	246	163	1238	1647
Cu	290	183	366	839
Total	4033	2441	11710	18184

not considered. This cutoff was chosen as a balance between prediction accuracy and computational cost. The CSM was applied to each absorbing site, and the polyhedron with the lowest CSM value was chosen as the site LCE label.

We restricted the LCE labels to only tetrahedral ($T4$), square pyramidal ($S5$), and octahedral ($O6$) geometries because across the eight transition-metal families these are the most abundant LCEs, often by an order of magnitude more than the rest. The class breakdown of the dataset is presented in Table I. The total number of site-specific spectra is on average a few thousand per atom type with V (3366) and Mn (3493) the most abundant and Cu (839) the least abundant. It should be noted that one can expand the dataset by adding new structures from other material databases generating artificial structures or introducing additional class labels. Furthermore, among all three chosen classes, $O6$ dominates, making up about 64% of the entire structure database. The impact of the inhomogeneity of the data distribution on the predictive power of the ML model is discussed in Sec. III.

C. Training machine learning models

The core machine learning algorithm (see Fig. 1) consists of an optional one-dimensional (1D) convolutional layer followed by three fully connected feedforward hidden layers with 90, 60, and 20 neurons, ending with a softmax output layer of three neurons. The input layer of the neural network is the XANES spectrum scaled to zero mean and unit variance on a standardized grid of 100 entries, and the output determines the target vector, which contains the probabilities of the three LCE classes ($T4$, $S5$, and $O6$) computed from the softmax function. All neurons use the rectified linear unit (ReLU) activation function and a 30% dropout to guard against overfitting. ML models with and without the 1D convolutional layer are referred to as the convolutional neural network (CNN) and multilayer perceptron (MLP), respectively. The optional convolutional layer contains eight filters and a kernel (sliding window) size of ten, stride of one, and max-pooling size of two and takes as input spectral data processed in an identical manner to that of the MLP. CNNs inherently assume correlations between nearby data points, and being a down-sampling and pooling technique, sacrifice resolution in favor of invariance to the precise location of input data. The algorithm determines trained parameters by

minimizing a categorical cross-entropy loss function using the Adam optimizer [65]. Minibatch sizes of 32 were used during 50 full passes (epochs) of the training data. All training and evaluations were performed using Keras [66] with a TensorFlow [67] backend.

For each absorbing site, we used statistical bootstrapping: 90% of the database was used for training ML models and the remainder for testing. These subsets were selected randomly in a stratified manner, meaning that the proportion of each class in both the training and the testing sets was always the same. In order to generate a statistical estimate on the accuracy of the classifier, we sampled the testing data with replacement over ten folds and report the averaged results in Fig. 3. To make full use of all available information, data included once in a testing set were not used in any future testing sets. We found that testing results are mostly invariant to the chosen neural network architecture assuming enough training parameters were included. Therefore, the fixed three-layer MLP with an optional convolutional layer (and associated hyperparameters) was used throughout all computations.

III. RESULTS AND DISCUSSION

In the following, we present our LCE classification study through visual inspection, principal component analysis (PCA) [68] and analysis of the machine learning classifiers (MLCs). We demonstrate that MLCs can accurately predict LCE classes from synthetic XANES data generated by the FEFF9 code. We further discuss the relevance of this paper based on synthetic data to the real challenge of the LCE classification of experimentally measured XANES spectra.

A. Visual inspection of the spectral database

The FEFF K-edge XANES database of eight $3d$ transition-metal elements (from Ti to Cu) is shown in Fig. 2, color coded by the LCE class ($T4$: blue; $S5$: green; $O6$: red). There are noticeable trends in the raw spectra that can be detected by visual inspection, prior to a more in-depth analysis. Overall, early $3d$ transition metals (e.g., Ti, V, Cr, and Mn) show more intense preedge peaks than late $3d$ transition metals (e.g., Ni and Cu), consistent with the trend from experiment [17]. Notably, $T4$ in Ti, V, and Cr oxides exhibit sharp preedge peaks at about 4970, 5470, and 5995 eV, respectively. The preedge peak intensity decreases as the coordination number increases, consistent with the observations of Farges and co-workers [20–22] and Jackson *et al.* [23]. Such qualitative agreement between theory and experiment suggests that spectral analysis of the FEFF database is physically insightful especially for the LCE classification problem.

In addition to preedge features, across the eight elements $T4$ exhibits the highest *postedge* intensity, followed by $S5$ and finally by $O6$. However, the role of postedge features in the LCE classification has not yet been explored in the literature, which could be an important supplement to existing preedge-based methods. We expect that algorithms including a wide energy range in the XANES spectra can, in principle, improve the spectral sensitivity to the LCE as compared to those relying solely on preedge features.
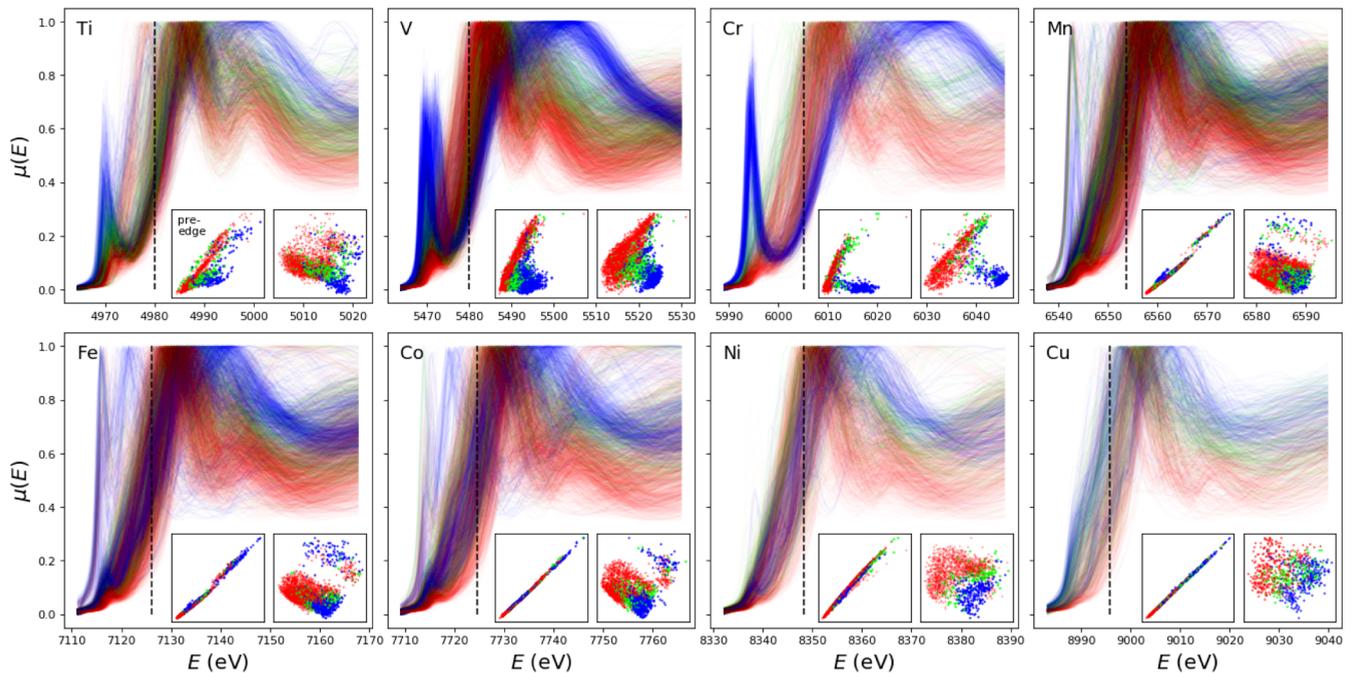
FIG. 2. FEFF K-edge XANES database of eight $3d$ transition-metal families. Spectra were spline interpolated onto discretized grids of 100 points and scaled on the vertical axis such that the maximum value is 1 (prior to shifting the mean to 0 and scaling to unit variance). The intensity of the colors scales inversely with the number of entries per class to aid visualization. Principal component analysis of two regions is shown in the two insets: the full feature space (lower right), and only the preedge region (lower center, discussed in Sec. III). The x and y axes correspond to the first and second principal axes. The cutoff for the preedge region is delineated by the vertical dashed line. Classes are color coded as follows: blue for tetrahedral ($T4$), green for square pyramidal ($S5$), and red for octahedral ($O6$).

B. Principal component analysis of the spectral database

We further analyzed the spectral database with PCA. Following the standard notation, X^k is defined as the full set of spectral data for the kth absorbing species with $\mathbf{x}^{jk}$ being the jth spectrum in the dataset (a single feature vector input) after taking zero sample mean and unit variance. Denote $\mathbf{w}^{1k}$ and $\mathbf{w}^{2k}$ as the first two principal axes in the feature space. We computed coordinates of spectrum j in the PCA plot $\mathbf{z}^{jk} = z_1^{jk}\hat{x} + z_2^{jk}\hat{y}$ as

$$z_\alpha^{jk} = \frac{\mathbf{x}^{jk} \cdot \mathbf{w}^{\alpha k}}{\max_l \left| z_\alpha^{lk} \right|}, \quad \alpha = 1, 2, \tag{1}$$

where for clarity the denominator scales z_α^{jk} within $[-1, 1]$.

To evaluate the significance of the preedge features, we truncated the principal axes by applying a cutoff n_c to the spectra such that $x_{n_c}^{jk}$ correspond to the vertical dashed lines in Fig. 2. Then PCA was performed for only the preedge region along the truncated principal axes,

$$\tilde{z}_\alpha^{jk} = \frac{\sum_{n=1}^{n_c} x_n^{jk} w_n^{\alpha k}}{\max_l \left| \tilde{z}_\alpha^{lk} \right|}, \quad \alpha = 1, 2, \tag{2}$$

by excluding features beyond $x_{n_c}^{jk}$. The axes in the plots generated by Eqs. (1) and (2) are scaled in the same way so that their clustering patterns can be compared directly. Similar patterns are expected from the full and preedge PCA plots if the preedge features dominate the spectral contrast. On the other hand, if the preedge features are less significant,

there will be weak correlations between two sets of PCA patterns.

Full PCA plots are shown in the lower right insets of Fig. 2. Overall, a large degree of clustering is realized, consistent with the observation of distinguishable spectral features from visual inspection. In Ti, V, Cr, Mn, Fe, and Co, most of the $T4$ points are located in the lower right corner, and the $O6$ points are located in the upper left corner. The $T4$ and $O6$ points of Ti, V, and Cr can be easily separated in PCA plots due to their sharp ($T4$) and negligible ($O6$) preedge features. In the PCA plots of Mn, Fe, and Co, there is also a secondary cluster of $T4$ points located in the upper right corner. The data distributions in Ni and Cu are similar to the others but with a slightly smaller packing density. In most cases, $S5$ clusters are intertwined with the other two classes, flanked by $T4$ on one side and $O6$ on the other.

The lower center insets in Fig. 2 show the PCA of the preedge region. All classes appear less clustered than the PCA patterns of the full feature space. Although in this case information contained in the feature space has clearly been reduced, this effect is less prominent in the early transition-metal elements, which still exhibit a large degree of clustering due to the significant spectral contrast in the preedge region. On the contrary, elements, such as Co, Ni, and Cu exhibit such severe information loss that PCA data points collapse into a linear pattern, which is detrimental to the MLC performance, especially in systems that already exhibit weak spectral contrast.

To summarize, visual inspection and PCA suggest that a MLC is likely able to accurately learn the trends in XANES

spectra and correlate them to their respective classes. However, it is unclear whether MLCs can perform equally well for every class in all of the transition-metal species we studied.

C. Machine learning classifier performance

The accuracy of the MLCs for each LCE class is reported using the F_1 score, which is the harmonic mean of the precision P and recall R,

$$F_1 = \frac{2PR}{P+R}, \quad P = \frac{t_+}{t_+ + f_+}, \quad R = \frac{t_+}{t_+ + f_-}, \quad (3)$$

where t_+, f_+, and f_- represent the true positives, false positives, and false negatives in a two-class (2×2) confusion matrix.

In order to make a fair assessment of the MLC performance, we need to address the data imbalance issue in our training set. As seen in Table I, the number of LCEs that conform to the $O6$ geometry vastly outnumbers the others, indicating that the accuracy of each class alone might not be the most reliable metric as it may be biased due to class imbalances in the training data. We address this problem in two ways: by using the F_1 score instead of the accuracy on a class-by-class basis, and reporting the macro F_1 score ($\overline{F}_1$) as a representative metric.

In general, the F_1 score is a much stricter metric than the accuracy and is a better indicator of performance. It accounts for both the precision P (of all predicted positives, cases that are actually positive) and the recall R (out of all the actual positives, cases that are correctly identified) and dramatically penalizes poor scores in either category (contrary to the mean of the precision and recall). To demonstrate why this is important, consider the F_1 score of the relatively underrepresented $S5$ class. Suppose that there are 10 $S5$ and 100 $T4$ and $O6$ in the dataset and that the classifier has a 10% false negative and false positive rate. Accuracy would naturally be 90%, but this is a poor representation of the classifier since ten non-$S5$ data points were predicted as $S5$, unnaturally inflating the number of predicted positives. On the contrary, the F_1 score of 62% accounts for this by incorporating the low precision (47%) into the metric. In addition to a breakdown by class, the macro F_1 score is reported, which is the average of the classwise F_1 scores computed using a one-versus-all approach. The $\overline{F}_1$ score treats each class on equal footing and further penalizes classifying data in an underrepresented class incorrectly relative to a class with many data points.

As clearly shown from the $\overline{F}_1$ scores in Table II, MLCs can classify the LCEs of all eight $3d$ transition-metal families very accurately. Uncertainties reported in the last digit of Table II and error bars in Fig. 3 correspond to the standard deviation calculated from ten different trained models. CNNs and MLPs perform equally well with very close $\overline{F}_1$ scores of 0.86 and 0.85, respectively. The classwise F_1 scores are plotted in Fig. 3. Notably, MLCs can reach over 90% accuracy on the $T4$ (CNN: 0.92; MLP: 0.92) and $O6$ classes (CNN: 0.96; MLP: 0.95), which can be understood from the observation of raw spectra. The strong preedge peak intensity is a signature of the $T4$ configuration in, e.g., Ti, V, and Cr. Conversely, the lack of a significant preedge peak is a clear indicator of an

TABLE II. $\overline{F}_1$ scores for different absorbing species, as the averages of the classwise F_1 scores (red, green and blue bars) presented in Fig. 3 both with (CNN) and without (MLP) the convolutional layer. Comparisons are made between models trained from the full feature space and reduced feature space corresponding to only the preedge region of the spectra.

Element	Full feature space		Preedge only	
	MLP	CNN	Pre-MLP	Pre-CNN
Ti	0.83(2)	0.84(2)	0.73(4)	0.78(3)
V	0.86(1)	0.86(2)	0.77(2)	0.79(3)
Cr	0.87(2)	0.87(3)	0.72(4)	0.75(4)
Mn	0.83(2)	0.85(2)	0.62(4)	0.68(3)
Fe	0.85(2)	0.86(3)	0.57(2)	0.63(3)
Co	0.85(3)	0.87(2)	0.59(3)	0.64(3)
Ni	0.87(1)	0.88(3)	0.61(5)	0.66(4)
Cu	0.86(2)	0.86(2)	0.50(4)	0.64(7)
Average	0.85(1)	0.86(1)	0.64(1)	0.70(1)

$O6$ configuration. In these cases, it is likely that the preedge features are sufficient to distinguish $O6$ from $T4$. On the contrary, the spectral contrast between $T4$ and $O6$ is very low in the preedge region in late transition-metal elements especially in Ni and Cu. It is remarkable that MLCs can achieve the same accuracy for $T4$ and $O6$ in late transition-metal elements. Such a universally good performance underscores the ability of the MLCs to extract spectral descriptors without human bias in the full energy range, including the pre-, main-, and postedge regions. Moreover, the relatively small overall error margin is a testament to the reliability and robustness of the classifier across many trained models.

Relative to $T4$ and $O6$, the $S5$ classification is less successful, with an overall accuracy of ~0.70 (CNN: 0.71; MLP: 0.68) as shown in Fig. 3. The weaker performance of MLCs on the $S5$ class can be explained by Fig. 2 where data associated with the $S5$ class lay between those in $T4$ and $O6$ in both the spectral and the principal component spaces, making them more difficult to identify.

D. Importance of features beyond the preedge

The ability of MLCs to accurately classify late transition-metal oxides that lack prominent preedge features suggests that features beyond the preedge region play an important role in the neural network model. This hypothesis is supported by the PCA results shown in the insets of Fig. 2. In the late transition metals, although the full spectra can be effectively clustered in two-component PCA, the same analysis of preedge spectra displays a completely different linear pattern resulting from substantial information loss.

To gain further insight, we train MLCs with identical architectures using *only* the preedge region defined by energies below the dashed lines in Fig. 2, which we refer to as the pre-MLCs (pre-CNNs and pre-MLPs). In principle, if $\overline{F}_1$ scores of the pre-MLCs are close to those trained on the full spectra, then the preedge features are sufficient to classify the LCE for that absorbing element. Conversely, a significant drop in the $\overline{F}_1$ scores of the pre-MLCs would be a clear indication that
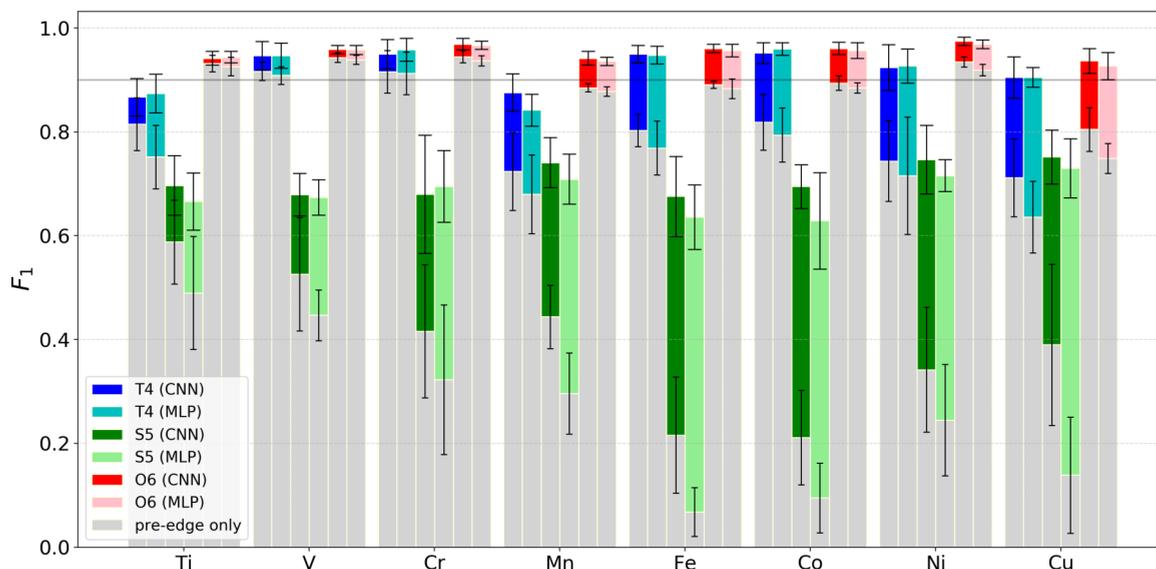
FIG. 3. Classwise F_1 scores calculated using different machine learning models (CNN/MLP) for $T4$ (blue/cyan), $S5$ (green/light green), and $O6$ (red/pink) local coordination environments in eight $3d$ transition-metal elements. The full height of each bar represents the results trained on the full feature space, while the gray bars overlaid on top with lower-F_1 values represent the results for the models trained only on the preedge region. For example, for the Co $S5$ CNN, the F_1 score reported for training on the full spectral space is about 0.7 but decreases sharply to about 0.2 when trained on the preedge region only. Error bars correspond to standard deviation; the ones with wider caps correspond to the full feature space.

features beyond the preedge region play a significant role in the MLCs.

As shown in Table II, the average $\overline{F}_1$ score in pre-MLCs drops significantly by about 20% (from 0.86 to 0.70 in CNN and from 0.85 to 0.64 in MLP) as compared to MLCs trained on the full spectral space. The classwise F_1 scores of pre-MLCs which are consistently lower than that of regular MLCs are shown in Fig. 3 as the gray bars. We quantify this accuracy degradation by

$$\Delta = F_1(\text{MLC}) - F_1(\text{pre-MLC})$$

and summarize the results averaged over early (Ti, V, Cr, and Mn) and late transition-metal elements (Fe, Co, Ni, and Cu) in Table III. First, Δ in late transition metals is more than doubled compared to early transition metals. Second, among the three classes, Δ of $O6$ is the smallest (< 0.10). It increases significantly for $T4$ in late transition metals to 0.16 in the pre-CNN (0.21 in the pre-MLP) and finally reaches the largest values for $S5$ at 0.22 (0.30) in early transition metals and 0.44 (0.57) in late transition metals. The results in Fig. 3 and Tables II and III highlight the critical importance of features beyond the preedge region in accurately classifying LCEs

TABLE III. The classwise difference between the F_1 scores evaluated over the entire feature space and over only the preedge region (Δ). Results are averaged over the early (Ti, V, Cr, and Mn) and late (Fe, Co, Ni, and Cu) transition-metal elements.

	pre-MLP			pre-CNN		
	$T4$	$S5$	$O6$	$T4$	$S5$	$O6$
Early	0.09(3)	0.30(5)	0.03(1)	0.07(3)	0.22(5)	0.03(1)
Late	0.21(4)	0.57(5)	0.10(1)	0.16(3)	0.44(7)	0.08(1)

especially for late transition metals. The effects are the largest in the $S5$ class, which is rather characterless in the preedge region, showing neither very strong (such as $T4$) nor very weak (such as $O6$) preedge intensities.

We note that, unlike the case of regular MLCs, the preedge CNN averaged over all absorbing species ($\overline{F}_1 = 0.70$) outperforms the corresponding preedge MLP ($\overline{F}_1 = 0.64$) substantially. In the most extreme situation of $S5$, the pre-CNN ($F_1 = 0.48$) is 23% more accurate than the pre-MLP ($F_1 = 0.39$) in early transition metals, and it is more than doubled in late transition metals with $F_1 = 0.28$ (0.12) for the pre-CNN (pre-MLP). The substantially better performance of the pre-CNN is likely caused by the use of the convolutional filter, which makes the CNN able to learn subtle preedge features from augmented data more effectively than the MLP.

E. Discussion

The MLCs described so far were trained on computational FEFF XANES spectra. Developing MLCs that can classify the LCE of a broad range of material families using experimental XANES spectra is a more challenging task that is beyond the scope of the current paper. Nonetheless, in this section we discuss several key issues that need to be addressed in order to achieve this goal, including validation of the theory, edge alignment of the simulated spectra, and the variations in the spectral intensity.

In order to apply MLCs trained on synthetic data to experimental spectra, it is very important to validate the theory such that the computational spectra can faithfully reproduce experimental spectral features. To this end, we compare FEFF spectra with experimental spectra on a small number of oxides: $K_6Ti_2O_7$, rutile (TiO_2), $MnCr_2O_4$, $MnCO_3$, $CoAlO_4$, and $Co(AsO_4)_2$ in Fig. 4. This list is not meant to be
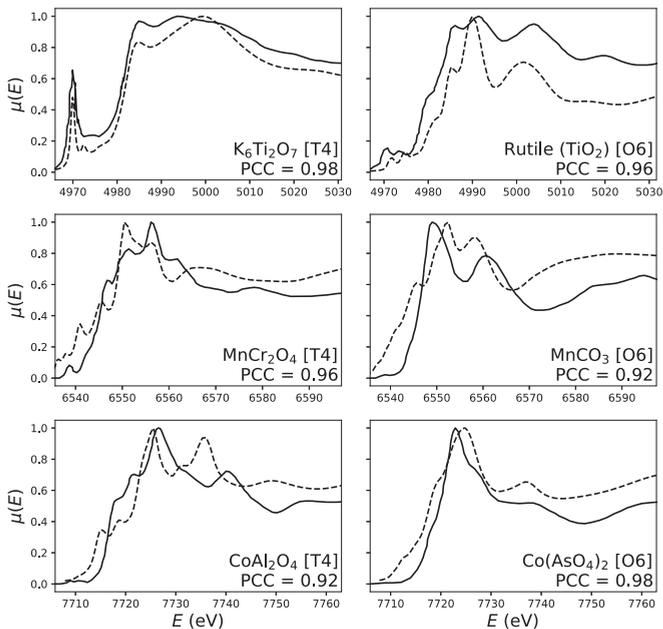
FIG. 4. Comparison between representative experimental (solid) and FEFF (dashed) XANES spectra. FEFF calculations are shifted on the energy axis to maximize the Pearson correlation coefficient (PCC) in order to find the best match between experimental and theoretical XANES. The experimental spectra of $K_6Ti_2O_7$ and rutile were extracted from Farges *et al.* [21], and the experimental spectra of both pairs of Mn and Co oxides were extracted from Manceau *et al.* [69].

FIG. 5. $\overline{F}_1$ score as a function of the amount of energy shift (ΔE) applied to the test set. The two graphs on the left illustrate the results of MLCs trained on augmented data (as presented thus far: ± 1 and 2 eV, generating five times the base amount of training data), whereas those on the right illustrate MLCs trained without augmenting the training set.

exhaustive. Within this small sample, although the overall shape and major peaks are well reproduced by FEFF, there are noticeable differences in the spectral details, including the peak positions and relative intensities of different peaks. Furthermore, the degree of agreement is system dependent. As shown in Fig. 4, the optimal PCCs between FEFF and experiment range from 0.92 to 0.98.

Despite the relatively high PCC scores, MLCs trained on spectra at the FEFF level of theory as such cannot reliably classify experimental spectra. It is necessary to generate the computational XANES database with more accurate methods and conduct a systematic benchmark of theory against experiment. However, the computational expense of these calculations grows quickly with the complexity of the methods, which could, in practice, limit the level of theory used to generate the training set. A good compromise would involve developing robust ML algorithms for a physically sound but numerically imperfect training set. It may also be possible to augment the computational spectral database with a subset of experimental data and apply ML techniques that can handle a hybrid database, such as transfer learning.

Another open question in computational XANES is the edge alignment of computational spectra with experimental spectra because current first-principles electronic structure methods have difficulty predicting accurate absolute onset energies. This issue stems from the use of pseudopotentials and/or approximations to the electron self-energy and core-hole final-state effects. Therefore, XANES calculations are often analyzed with the relative energy scale, or after they are
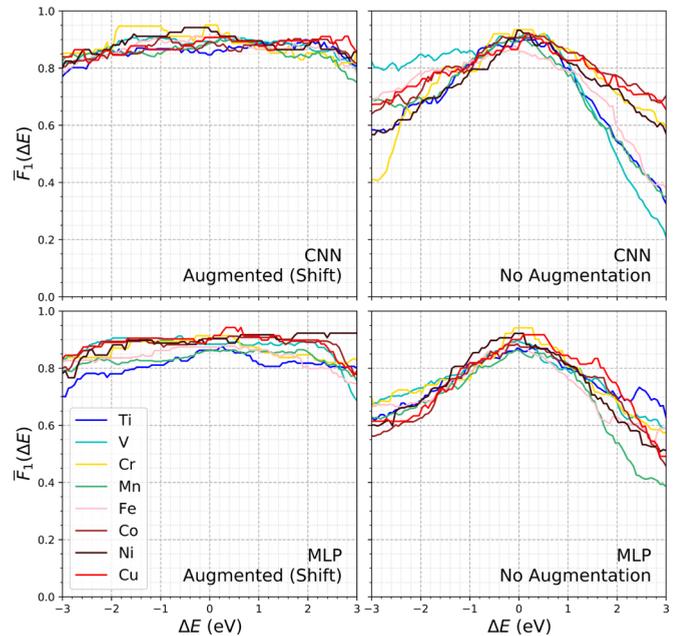
manually aligned with reference experimental spectra. However, the energy shift in the spectral alignment with respect to reference experimental spectra could be system dependent, which warrants further study.

In order to investigate the impact of the edge alignment on the performance of MLCs, we shift the test set by up to ± 3 eV to study the transferability of MLCs against the shifted data. We note that a shift of 3 eV in energy is quite significant as the energy range of the preedge region is about 10–15 eV. As shown in Fig. 5, the MLCs are very robust against the energy shift as the $\overline{F}_1(\Delta E)$ curves are almost flat. The CNN slightly outperforms MLP with $\overline{F}_1(CNN) > 0.8$ in most of the range of ΔE for all eight elements. The robustness of the MLCs results from the data augmentation we applied in the training set with energy shifts of ± 1 and ± 2 eV as described in Sec. II. If we apply the same test on MLCs developed from the base training set without data augmentation, the accuracy deteriorates quickly after $|\Delta E| > 1$ eV as shown in Fig. 5.

Additionally, we have seen that the spectral intensity of theoretical XANES spectra may not match perfectly with experiments. On top of that, the intensity of experimental XANES spectra is subject to several uncertainties from sample preparation and various instrumental factors, such as type and mosaic spread of the monochromator crystals, source sizes, slit heights, and beam instabilities [21] and the resolution of the apparatus [70]. Therefore, experimental spectra of the same materials that are measured using different samples or collected at different beamline settings may have slightly different intensity profiles. To investigate the impact of the uncertainties in the spectral intensity on the MLCs, we introduced Gaussian random noise with standard deviation
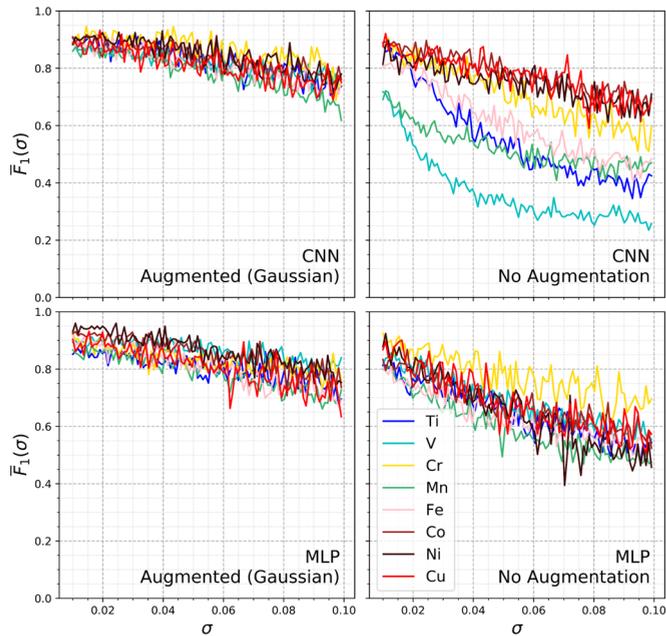
FIG. 6. $\overline{F}_1$ score as a function of the standard deviation (σ) used to generate Gaussian random noise, introduced into every point E in the spectra $\mu(E)$. The two graphs on the left illustrate the results of MLCs trained on a training set augmented with Gaussian random noise of $\sigma = 0.03$ (also generating five times the base amount of training data), and those on the right illustrate MLCs trained without data augmentation.

σ to the spectral intensity centered around $\mu(E)$ for every E on the energy grid. To isolate the effects of the Gaussian random noise, we test the MLCs trained without augmentation accounting for the energy shift. As shown in Fig. 6, the overall $\overline{F}_1$ score decays quickly with the increasing σ in both the CNN and the MLP with V trained using the CNN suffering the most. After we augmented the training set with spectra containing the Gaussian random noise with $\sigma = 0.03$, the $\overline{F}_1$ score decays much more slowly with increasing σ.

From the analysis above, one can clearly see that MLCs perform dramatically better when the training set is augmented, which is a sensible result. It is interesting to note that the CNN underperforms relative to the MLP without data augmentation, specifically for early transition metals that exhibit strong preedge peaks. For example, the $\overline{F}_1$ score of the unaugmented CNN for Ti and V drops to ~ 0.45 and 0.25, respectively, at $\sigma = 0.1$. This trend is not entirely counterintuitive for two reasons. First, the CNN as described

in Sec. II C is not completely shift invariant, and without proper data augmentation it may not learn how to account for small perturbations. Second, as shown in Table III, the CNN relies more on the preedge region than the MLP. Since shifting the location of the preedge peak strongly affects the preedge spectral features, a sizable drop in performance is to be expected. A similar argument may be made for the effects of Gaussian random noise, which can artificially distort both the shape and the location of the peaks.

IV. CONCLUSION

We propose a computational framework to perform element-specific classification of local chemical environments from XANES spectra. In addition to the construction of structural databases, spectral databases, and structural labels, a central element of this framework is unraveling the correlation between spectral features and local chemical environments systematically using machine learning classifiers. As a proof of principle, we applied our method to the computational XANES database of eight $3d$ transition-metal elements generated by the FEFF code and achieved a high average macro F_1 score of 0.86. Our method can reliably capture not only the prominent preedge features, but also the less characteristic spectral features beyond the preedge region. We showed that features beyond the preedge region turn out to be very important to the accuracy of the classification especially for late transition-metal elements. The ability to extract key structural information in the full spectral range makes our machine learning-based method more robust and transferable than empirical fingerprint methods based solely on the preedge region. As an important starting point, our paper will motivate future research on the problem of classification of local chemical environments on experimental measured spectra.

[1] J. D. Jorgensen, M. A. Beno, D. G. Hinks, L. Soderholm, K. J. Volin, R. L. Hitterman, J. D. Grace, I. K. Schuller, C. U. Segre, K. Zhang, and M. S. Kleefisch, Phys. Rev. B **36**, 3608 (1987).

[2] A. Cavalleri, C. Tóth, C. W. Siders, J. A. Squier, F. Ráksi, P. Forget, and J. C. Kieffer, Phys. Rev. Lett. **87**, 237401 (2001).

[3] B. Kang and G. Ceder, Nature (London) **458**, 190 (2009).

[4] H. Peng, P. F. Ndione, D. S. Ginley, A. Zakutayev, and S. Lany, Phys. Rev. X **5**, 021016 (2015).

[5] D. P. Tabor, L. M. Roch, S. K. Saikin, C. Kreisbeck, D. Sheberla, J. H. Montoya, S. Dwaraknath, M. Aykol, C. Ortiz, H. Tribukait *et al.*, Nat. Rev. Mater. **3**, 5 (2018).

[6] J. E. Gubernatis and T. Lookman, Phys. Rev. Mater. **2**, 120301 (2018).

[7] F. Meirer and B. M. Weckhuysen, Nat. Rev. Mater. **3**, 324 (2018).

[8] A. Ankudinov, J. Rehr, J. J. Low, and S. R. Bare, J. Chem. Phys. **116**, 1911 (2002).

[9] J. J. Rehr, J. J. Kas, M. P. Prange, A. P. Sorini, Y. Takimoto, and F. Vila, C. R. Phys. **10**, 548 (2009).

[10] A. I. Frenkel, J. A. Rodriguez, and J. G. Chen, ACS Catal. **2**, 2269 (2012).

[11] A. L. Ankudinov, B. Ravel, J. J. Rehr, and S. D. Conradson, Phys. Rev. B **58**, 7565 (1998).

[12] D. Bazin and J. J. Rehr, J. Phys. Chem. B **107**, 12398 (2003).

[13] G. Ciatto, A. Di Trolio, E. Fonda, P. Alippi, A. M. Testa, and A. A. Bonapasta, Phys. Rev. Lett. **107**, 127206 (2011).

[14] Q. Ma, J. Prater, C. Sudakar, R. Rosenberg, and J. Narayan, J. Phys.: Condens. Matter **24**, 306002 (2012).

[15] A. Kuzmin and J. Chaboy, IUCrJ **1**, 571 (2014).

[16] U. Srivastava and H. Nigam, Coord. Chem. Rev. **9**, 275 (1973).

[17] T. Yamamoto, X-Ray Spectrom. **37**, 572 (2008).

[18] H. Hanson and W. W. Beeman, Phys. Rev. **76**, 118 (1949).

[19] J. Wong, F. W. Lytle, R. P. Messmer, and D. H. Maylotte, Phys. Rev. B **30**, 5596 (1984).

[20] F. Farges, G. E. Brown, Jr., and J. J. Rehr, Geochim. Cosmochim. Acta **60**, 3023 (1996).

[21] F. Farges, G. E. Brown, Jr., and J. J. Rehr, Phys. Rev. B **56**, 1809 (1997).

[22] F. Farges, G. E. Brown, Jr., P.-E. Petit, and M. Munoz, Geochim. Cosmochim. Acta **65**, 1665 (2001).

[23] W. E. Jackson, F. Farges, M. Yeager, P. A. Mabrouk, S. Rossano, G. A. Waychunas, E. I. Solomon, and G. E. Brown, Geochim. Cosmochim. Acta **69**, 4315 (2005).

[24] F. A. Cotton and C. J. Ballhausen, J. Chem. Phys. **25**, 617 (1956).

[25] F. A. Cotton and H. P. Hanson, J. Chem. Phys. **25**, 619 (1956).

[26] G. Mountjoy, D. M. Pickup, G. Wallidge, R. Anderson, J. M. Cole, R. J. Newport, and M. E. Smith, Chem. Mater. **11**, 1253 (1999).

[27] S. Bordiga, E. Groppo, G. Agostini, J. A. van Bokhoven, and C. Lamberti, Chem. Rev. **113**, 1736 (2013).

[28] N. Jiang, D. Su, and J. C. H. Spence, Phys. Rev. B **76**, 214117 (2007).

[29] S. Yoshida, T. Tanaka, T. Hanada, T. Hiraiwa, H. Kanai, and T. Funabiki, Catal. Lett. **12**, 277 (1992).

[30] T. Tanaka, H. Yamashita, R. Tsuchitani, T. Funabiki, and S. Yoshida, J. Chem. Soc., Faraday Trans. 1 **84**, 2987 (1988).

[31] W. Zhang, M. Topsakal, C. Cama, C. J. Pelliccione, H. Zhao, S. Ehrlich, L. Wu, Y. Zhu, A. I. Frenkel, K. J. Takeuchi *et al.*, J. Am. Chem. Soc. **139**, 16591 (2017).

[32] G. Carleo and M. Troyer, Science **355**, 602 (2017).

[33] E. P. L. van Nieuwenburg, Y.-H. Liu, and S. D. Huber, Nat. Phys. **13**, 435 (2017).

[34] J. Behler and M. Parrinello, Phys. Rev. Lett. **98**, 146401 (2007).

[35] J. R. Kitchin, Nat. Catal. **1**, 230 (2018).

[36] J. Timoshenko, D. Lu, Y. Lin, and A. I. Frenkel, J. Phys. Chem. Lett. **8**, 5091 (2017).

[37] J. Timoshenko, A. Anspoks, A. Cintins, A. Kuzmin, J. Purans, and A. I. Frenkel, Phys. Rev. Lett. **120**, 225502 (2018).

[38] A. Jain, S. P. Ong, G. Hautier, W. Chen, W. D. Richards, S. Dacek, S. Cholia, D. Gunter, D. Skinner, G. Ceder, and K. A. Persson, APL Mater. **1**, 011002 (2013).

[39] S. P. Ong, W. D. Richards, A. Jain, G. Hautier, M. Kocher, S. Cholia, D. Gunter, V. L. Chevrier, K. A. Persson, and G. Ceder, Comput. Mater. Sci. **68**, 314 (2013).

[40] S. P. Ong, S. Cholia, A. Jain, M. Brafman, D. Gunter, G. Ceder, and K. A. Persson, Comput. Mater. Sci. **97**, 209 (2015).

[41] J. J. Rehr and R. C. Albers, Rev. Mod. Phys. **72**, 621 (2000).

[42] M. Taillefumier, D. Cabaret, A.-M. Flank, and F. Mauri, Phys. Rev. B **66**, 195107 (2002).

[43] C. Gougoussis, M. Calandra, A. Seitsonen, C. Brouder, A. Shukla, and F. Mauri, Phys. Rev. B **79**, 045118 (2009).

[44] D. Prendergast and G. Galli, Phys. Rev. Lett. **96**, 215502 (2006).

[45] W. Chen, X. Wu, and R. Car, Phys. Rev. Lett. **105**, 017802 (2010).

[46] J. Vinson, J. J. Rehr, J. J. Kas, and E. L. Shirley, Phys. Rev. B **83**, 115106 (2011).

[47] J. Vinson, T. Jach, W. T. Elam, and J. D. Denlinger, Phys. Rev. B **90**, 205207 (2014).

[48] A. Gulans, S. Kontur, C. Meisenbichler, D. Nabok, P. Pavone, S. Rigamonti, S. Sagmeister, U. Werner, and C. Draxl, J. Phys.: Condens. Matter **26**, 363202 (2014).

[49] C. Vorwerk, C. Cocchi, and C. Draxl, Phys. Rev. B **95**, 155121 (2017).

[50] Y. Liang, J. Vinson, S. Pemmaraju, W. S. Drisdell, E. L. Shirley, and D. Prendergast, Phys. Rev. Lett. **118**, 096402 (2017).

[51] Z. Sun, L. Zheng, M. Chen, M. L. Klein, F. Paesani, and X. Wu, Phys. Rev. Lett. **121**, 137401 (2018).

[52] J. Timoshenko, C. J. Wrasman, M. Luneau, T. Shirman, M. Cargnello, S. R. Bare, J. Aizenberg, C. M. Friend, and A. I. Frenkel, Nano Lett. **19**, 520 (2019).

[53] M. W. Small, J. J. Kas, K. O. Kvashnina, J. J. Rehr, R. G. Nuzzo, M. Tromp, and A. I. Frenkel, ChemPhysChem **15**, 1569 (2014).

[54] J. Timoshenko, A. Shivhare, R. W. J. Scott, D. Lu, and A. I. Frenkel, Phys. Chem. Chem. Phys. **18**, 19621 (2016).

[55] H. Singh, M. Topsakal, K. Attenkofer, T. Wolf, M. Leskes, Y. Duan, F. Wang, J. Vinson, D. Lu, and A. I. Frenkel, Phys. Rev. Mater. **2**, 125403 (2018).

[56] K. Mathew, C. Zheng, D. Winston, C. Chen, A. Dozier, J. J. Rehr, S. P. Ong, and K. A. Persson, Sci. Data **5**, 180151 (2018).

[57] C. Zheng, K. Mathew, C. Chen, Y. Chen, H. Tang, A. Dozier, J. J. Kas, F. D. Vila, J. J. Rehr, L. F. Piper *et al.*, npj Comput. Mater. **4**, 12 (2018).

[58] D. Yan, M. Topsakal, S. Selcuk, J. Lyons, W. Zhang, Q. Wu, I. Waluyo, E. Stavitski, K. Attenkofer, S. Yoo, D. Lu, M. Hybertsen, D. Stacchiola, and M. Liu (unpublished).

[59] J. Rehr, J. Kas, F. Vila, M. Prange, and K. Jorissen, Phys. Chem. Chem. Phys. **12**, 5503 (2010).

[60] M. Rupp, A. Tkatchenko, K.-R. Müller, and O. A. von Lilienfeld, Phys. Rev. Lett. **108**, 058301 (2012).

[61] J. S. Smith, O. Isayev, and A. E. Roitberg, Chem. Sci. **8**, 3192 (2017).

[62] S. Chmiela, A. Tkatchenko, H. E. Sauceda, I. Poltavsky, K. T. Schütt, and K.-R. Müller, Sci. Adv. **3**, e1603015 (2017).

[63] M. Pinsky and D. Avnir, Inorg. Chem. **37**, 5575 (1998).

[64] D. Waroquiers, X. Gonze, G.-M. Rignanese, C. Welker-Nieuwoudt, F. Rosowski, M. Göbel, S. Schenk, P. Degelmann, R. André, R. Glaum, and G. Hautier, Chem. Mater. **29**, 8346 (2017).

[65] D. P. Kingma and J. Ba, arXiv:1412.6980.

[66] F. Chollet *et al.*, KERAS, https://keras.io (2015).

[67] M. Abadi, A. Agarwal, P. Barham, E. Brevdo, Z. Chen, C. Citro, G. S. Corrado, A. Davis, J. Dean, M. Devin, S. Ghemawat, I. Goodfellow, A. Harp, G. Irving, M. Isard, Y. Jia, R. Jozefowicz, L. Kaiser, M. Kudlur, J. Levenberg, D. Mané, R. Monga, S. Moore, D. Murray, C. Olah, M. Schuster, J. Shlens, B. Steiner, I. Sutskever, K. Talwar, P. Tucker, V. Vanhoucke, V. Vasudevan, F. Viégas, O. Vinyals, P. Warden, M. Wattenberg, M. Wicke, Y. Yu, and X. Zheng, software available from tensorflow.org (2015).

[68] K. Pearson, Philos. Mag. **2**, 559 (1901).

[69] A. Manceau, A. I. Gorshkov, and V. A. Drits, Am. Mineral **77**, 1133 (1992).

[70] H. Yoshitake, T. Sugihara, and T. Tatsumi, Phys. Chem. Chem. Phys. **5**, 767 (2003).